The Astronomical Journal, 156:261 (9pp), 2018 December https://doi.org/10.3847/1538-3881/aae88f

Spitzer Observations of Interstellar Object 1I/'Oumuamua

David E. Trilling[1,2], Michael Mommert[1,2], Joseph L. Hora[3], Davide Farnocchia[4], Paul Chodas[4], Jon Giorgini[4], Howard A. Smith[3], Sean Carey[5], Carey M. Lisse[6], Michael Werner[4], Andrew McNeill[1], Steven R. Chesley[4], Joshua P. Emery[7], Giovanni Fazio[3], Yanga R. Fernandez[8], Alan Harris[9], Massimo Marengo[10], Michael Mueller[11,12], Alissa Roegge[1], Nathan Smith[1], H. A. Weaver[6], Karen Meech[13], and Marco Micheli[14]

[1] Department of Physics and Astronomy P.O. Box 6010 Northern Arizona University Flagstaff, AZ 86011, USA; david.trilling@nau.edu
[2] Lowell Observatory 1400 W. Mars Hill Road Flagstaff, AZ 86001, USA
[3] Harvard-Smithsonian Center for Astrophysics 60 Garden Street, MS-65 Cambridge, MA 02138, USA
[4] Jet Propulsion Laboratory, California Institute of Technology 4800 Oak Grove Drive Pasadena, CA 91101, USA
[5] IPAC, California Institute of Technology 1200 E. California Boulevard Pasadena, CA 91125, USA
[6] The Johns Hopkins University Applied Physics Laboratory 11100 Johns Hopkins Road Laurel, MD 20723-6099, USA
[7] Department of Earth & Planetary Science, University of Tennessee 306 EPS Building, 1412 Circle Drive Knoxville, TN 37996, USA
[8] Dept. of Physics & Florida Space Institute University of Central Florida 4000 Central Florida Boulevard, Orlando, FL 32816-2385, USA
[9] German Aerospace Center (DLR), Institute of Planetary Research Rutherfordstrasse 2, D-12489 Berlin, Germany
[10] Iowa State University, Department of Physics and Astronomy A313E Zaffarano Hall Ames, IA 50011, USA
[11] Kapteyn Astronomical Institute RijkSuniversiteit Groningen P.O. Box 800, 9700 AV Groningen, The Netherlands
[12] SRON, Netherlands Institute for Space Research P.O. Box 800, 9700AV Groningen, The Netherlands
[13] Institute for Astronomy 2680 Woodlawn Drive Honolulu, HI 96822, USA
[14] ESA SSA-NEO Coordination Centre Largo Galileo Galilei, 1 I-00044 Frascati (RM), Italy
Received 2018 July 13; revised 2018 October 4; accepted 2018 October 11; published 2018 November 14

Abstract

1I/'Oumuamua is the first confirmed interstellar body in our solar system. Here we report on observations of 'Oumuamua made with the *Spitzer Space Telescope* on 2017 November 21–22 (UT). We integrated for 30.2 hr at 4.5 μm (IRAC channel 2). We did not detect the object and place an upper limit on the flux of 0.3 μJy (3σ). This implies an effective spherical diameter less than [98, 140, 440] m and albedo greater than [0.2, 0.1, 0.01] under the assumption of low, middle, or high thermal beaming parameter η, respectively. With an aspect ratio for 'Oumuamua of 6:1, these results correspond to dimensions of [240:40, 341:57, 1080:180] m, respectively. We place upper limits on the amount of dust, CO, and CO_2 coming from this object that are lower than previous results; we are unable to constrain the production of other gas species. Both our size and outgassing limits are important because 'Oumuamua's trajectory shows non-gravitational accelerations that are sensitive to size and mass and presumably caused by gas emission. We suggest that 'Oumuamua may have experienced low-level post-perihelion volatile emission that produced a fresh, bright, icy mantle. This model is consistent with the expected η value and implied high-albedo value for this solution, but, given our strict limits on CO and CO_2, requires another gas species—probably H_2O—to explain the observed non-gravitational acceleration. Our results extend the mystery of 'Oumuamua's origin and evolution.

Key words: comets: individual (1I/'Oumuamua) – minor planets, asteroids: individual (1I/'Oumuamua) – planetary systems

1. Introduction

'Oumuamua (1I/2017 U1) was discovered on 2017 October 18. One week later it was announced that 'Oumuamua's orbit was unbound (Bacci et al. 2017) and that this was the first ever discovered interstellar body—an object that originated outside our solar system.

It has long been thought that comets and asteroids exist in other planetary systems. Most current models of our own solar system suggest that today's small bodies are leftovers from the era of planet formation (e.g., Dones et al. 2015), implying that other planetary systems also produced comet and/or asteroid populations. Until now, it has been impossible to connect our own local small-body populations to the large, but unresolved, groups of comets and asteroids found in exoplanetary circumstellar disks (e.g., Lisse et al. 2007, 2017).

'Oumuamua was the subject of an intense, though brief, observing campaign (Bannister et al. 2017; Jewitt et al. 2017; Knight et al. 2017; Masiero 2017; Meech et al. 2017; Ye et al. 2017; Belton et al. 2018; Bolin et al. 2018; Drahus et al. 2018; Fitzsimmons et al. 2018; Fraser et al. 2018; Micheli et al. 2018). In summary, 'Oumuamua has a red, featureless visible/near-infrared spectral slope, no directly-detected emission of gas or dust (though activity may be required to explain the presence of non-gravitational perturbations affecting its motion), a very elongated shape, and an excited rotation state. The color, spectral slope, density, and lack of apparent activity all suggest something like a D-type (primitive) asteroid, though the implied low-level activity points to a comet-like body. (The shape and rotation state do not particularly imply any specific analog in our solar system.) Assuming the object to have asteroidal density, McNeill et al. (2018) showed that no significant cohesive strength is required for 'Oumuamua to resist rotational fission, but even assuming a comet-like bulk density of 0.5 g cm^{-3} we find that a trivial cohesive strength of only 1 $\pm$ 1 Pa is required.

The existence of 'Oumuamua has implications for its formation and origin and on the small-body populations in other planetary systems (Trilling et al. 2017; Ćuk 2018; Do et al. 2018; Feng & Jones 2018; Gaidos 2018; Jackson et al. 2018; Katz 2018; Raymond et al. 2018a, 2018b; Zwart et al.

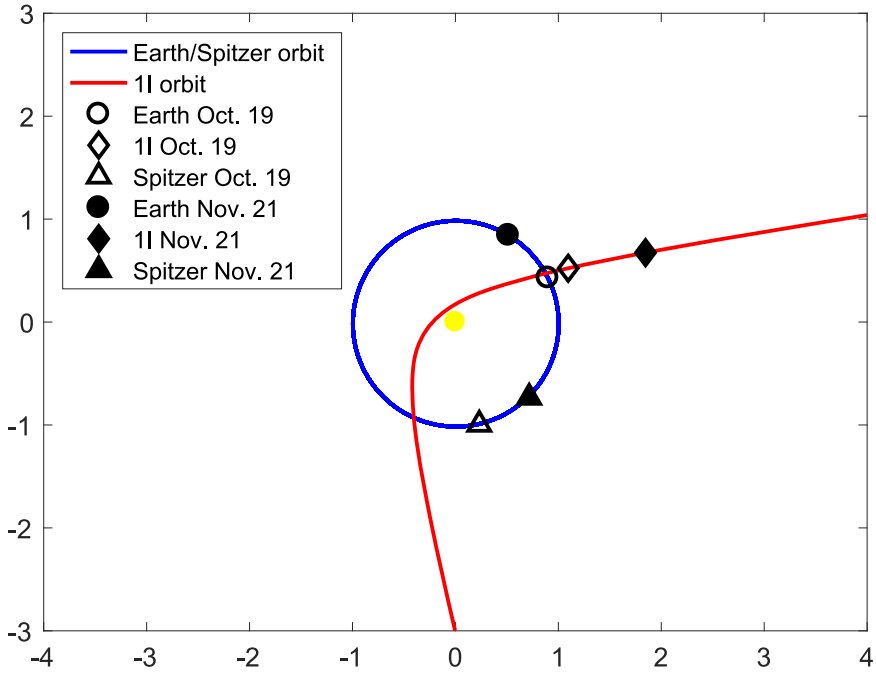

Figure 1. Sun-centered geometry (viewed from the north perpendicular of the ecliptic plane) of the Earth (circles), *Spitzer* (triangles), and ‘Oumuamua (diamonds) at the time of ‘Oumuamua’s discovery on 2017 October 19 (open symbols) and our *Spitzer* observations on 2017 November 21 (filled symbols). The *Spitzer* observability window is centered on 90° elongation (that is, perpendicular to the Sun-*Spitzer* line), so our *Spitzer* observations of this object could not be executed until late November. (Also, the few-week turnaround from observing request to execution was difficult to schedule; a smaller turnaround would not have been possible.) The orbits of Earth and *Spitzer* are shown as a blue (closed) circle; the hyperbolic orbit of ‘Oumuamua is shown in red. ‘Oumuamua was outbound at the time of discovery.

2018). Overall, these formation models generally prefer a comet-like body for interstellar interlopers.

As part of the observational campaign carried out before ‘Oumuamua became too faint, we observed this body with the *Spitzer Space Telescope*. *Spitzer* observations offered the best possibility to determine the diameter and albedo of this object by measuring its emitted thermal infrared radiation as our team has done for thousands of Near Earth Objects (NEOs; Trilling et al. 2010, 2016.)

Here we present the results of our *Spitzer* observations. We did not convincingly detect ‘Oumuamua and are left with an upper limit on its flux that corresponds to an upper limit on diameter and a lower limit on albedo. In Section 2, we present our observational approach and data reduction steps, details of the ephemeris and uncertainty calculations, and our observational results. In Section 3, we present our thermal modeling and the resulting limits on diameter and albedo, which strongly depend on choice of model parameters. We discuss our model results and search for activity in Section 4.

2. Observations and Results

2.1. Observations and Data Reduction

Observations were obtained with *Spitzer*/IRAC (Fazio et al. 2004) as part of DDT program 13249. Seven Astronomical Observing Requests (AORs) were used, six of ∼5 hr duration with 166 × 100 s frames, and a final 2.9 hr (clock time) AOR with 94 × 100 s frames, for a total of 1090 frames and 30.2 hr on-source frame time (acquired over 33 hr of clock time). The observations were divided in this way because of limits in the number of commands and data allowed in a single AOR. The data were taken with the “Moving Single” target mode with Full Array readouts, using a small cycling dither pattern. Two frames were taken at each dither position, to reduce the overhead of moving after each frame. Images were obtained in both arrays, but only the 4.5 μm channel was nominally centered on the target position, since the object was expected to be brighter in that IRAC channel. With the information known at that time, we estimated that with this integration time we could achieve a 3σ or better detection of the object if it was at its expected maximum brightness during the time of observation.

‘Oumuamua was discovered on 2017 October 19 (and announced as an interstellar body on 2017 October 25; Bacci et al. 2017), but because of the constraints of the *Spitzer* observability zone, the earliest that the *Spitzer* observations could begin was late on November 20 (Figure 1). The ephemeris used to develop the original *Spitzer* observation sequence was based on ground-based astrometric data through the end of October and had a prediction uncertainty larger than the *Spitzer* FOV. On November 9, the Magdalena Ridge Observatory collected additional ground-based observations, which we used together with preliminary high-precision astrometry from Micheli et al. (2018) to refine the orbit of ‘Oumuamua. We found that the revised predicted positions could potentially put the object very close to or off the edge of the array for many frames in the AORs constructed with the original ephemeris. The *Spitzer* Science Center (SSC) was able to replan the observations with the latest orbit information. The first AOR began executing at 2017 November 21 10:13:26 UT, and the last AOR completed at 2017 November 22 18:52:06 UT; this is around 2.5 months after ‘Oumuamua’s perihelion passage. The average heliocentric distance of ‘Oumuamua during the observations was 2.0 au and the average *Spitzer*-centric distance was 1.8 au; the average phase angle was around 31° (Figure 1). This geometry changed only very

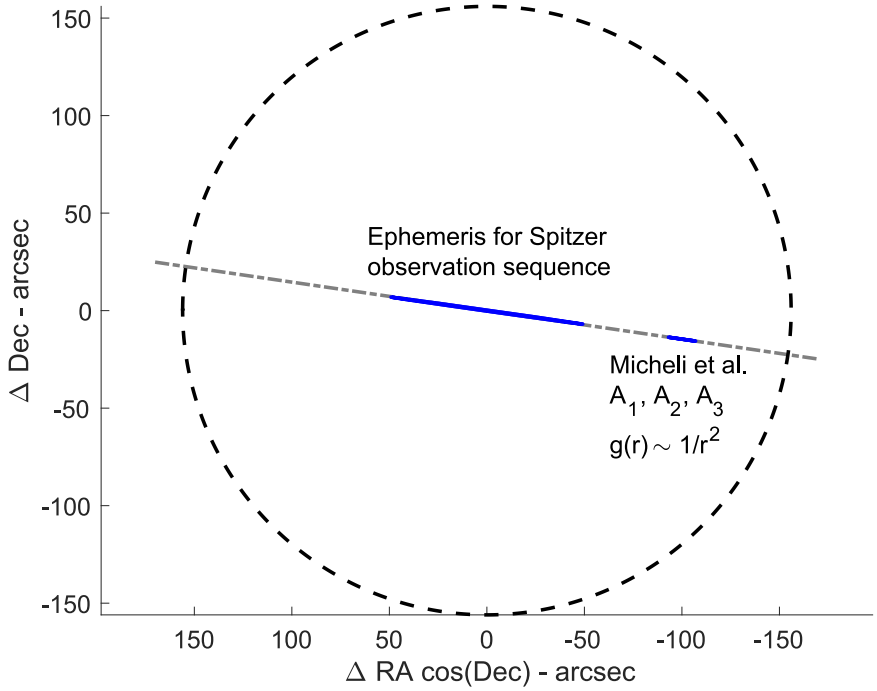

Figure 2. Plane-of-sky 3σ uncertainty ellipses on 2017 November 21.0 UT for the gravity-only ephemeris used to build the *Spitzer* sequence (blue solid portion in the center of the frame) and for the Micheli et al. (2018) solution (blue solid portion in the right of the frame), which has radial-transverse-normal non-gravitational accelerations (A_1, A_2, A_3) $g(r)$, $g(r) \propto 1/r^2$ (where r is the heliocentric distance). The dashed–dotted line is the Line of Variation, i.e., the direction of longest uncertainty. The dashed circle has a diameter of 5.2 arcmin and is therefore the inscribed circle of the *Spitzer* field of view. Thus, even when the non-gravitational accelerations that were not known at the time of our *Spitzer* observations are included, the location of "Oumuamua is still within the IRAC field of view. Even in the alternate and less-preferred Micheli et al. (2018) solutions of $1/r^k$ where $k = \{0, 1, 3\}$ 'Oumuamua would still be in the *Spitzer* field of view; the uncertainty represented by the red "inflated"' ellipse in Figure 3 captures these other solutions. Furthermore, the dithering that was used was sufficiently small that the nominal Micheli et al. (2018) location for the object still appears in all 1090 frames. Note that the ellipses shown here are so narrow that they appear to be lines in this figure.

slightly during the 33 hr of clock time needed to carry out these observations. The rate of motion on-sky in these observations was around 68 arcsec/hr.

The data reduction method used was similar to that described in Mommert et al. (2014b). A mosaic of the field was constructed from the data set itself and then subtracted from the individual basic calibrated data (BCD) frames. After subtraction of the background mosaic, residual background sources and bright cosmic ray artifacts were masked in the individual BCDs before being mosaicked in the reference frame of the moving object.

2.2. Ephemeris and Positional Uncertainties

Micheli et al. (2018) later collected ground-based and *Hubble Space Telescope* astrometry of 'Oumuamua, eventually extending the observational arc through 2018 January 2. Based on this longer sampling of the trajectory, they reported a 30σ detection of a non-gravitational acceleration acting on the motion of the object, inferred from position measurements over time. This acceleration was not visible or expected when the *Spitzer* observation sequence was built in November and would have resulted in an ephemeris correction of about 100 arcseconds at the time of the *Spitzer* observations (Figure 2). This correction is along the Line of Variation (Milani et al. 2005), i.e., the direction corresponding to the semimajor axis of the uncertainty ellipse, which corresponds to a position angle (north to east) of $81\overset{\circ}{.}8$. Though this correction is a statistically significant deviation (7.7σ) from the gravity-only ephemeris used to build the *Spitzer* observation sequence, the updated ephemeris still falls inside the *Spitzer* field of view, which is 5.2 arcmin on each side. The final mosaic presented below and our data analysis are based on the most recent solution for the position (i.e., Micheli et al. 2018), so the only impact on our observations between the pre-*HST* solution (used for planning our observations) and the post-*HST* solution would be the error in the rate over the individual 100 s integrations. The difference between the two solutions (i.e., the degree of trailing introduced) over that length of time is completely negligible.

2.3. Observational Results

Our final mosaic is shown in Figure 3 along with the predicted location of 'Oumuamua. There are no bright coherent sources in this image, so we conclude that we did not confidently detect the source. The 1σ noise level in the final mosaic is $\sim$0.1 μJy per PSF. This noise level was determined by recovering synthetic sources of various brightnesses that were injected in the final mosaic. Sources as faint as 0.3 μJy could be reliably found and extracted with an error of 0.1 μJy. This noise floor is consistent with our expectations from *Spitzer* observations of other very faint moving objects (Mommert et al. 2014a, 2014b).

There are several $\sim 2\sigma$ "blobs" (essentially, single pixels) in the image, and a "source" that is around 1σ that is located within the uncertainty ellipse. Since our final image is stacked in the moving frame of the target, the likelihood of any of these blobs corresponding to a different true astrophysical object, which would have to be moving at the same rate as "Oumuamua over 30 hr, is vanishingly small. Nevertheless, the presence of these blobs in the image at the 1σ or 2σ level

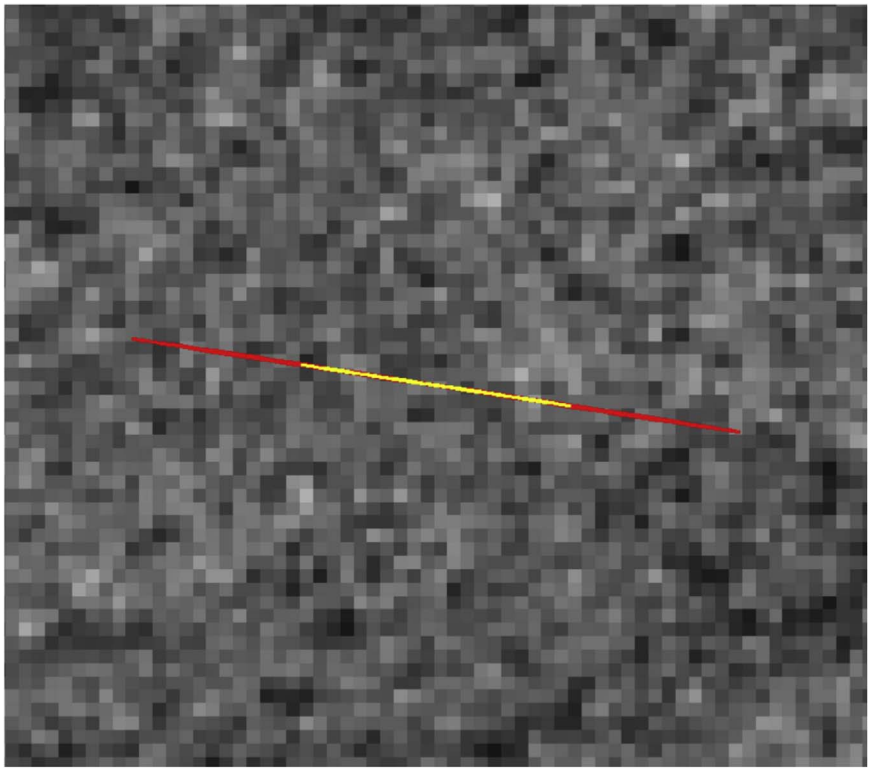

Figure 3. Final combined mosaic of all IRAC Channel 2 (4.5 μm) frames in the moving frame of 'Oumuamua using z-scale pixel scaling. Sidereal sources are removed before this stacked moving image is created, so there are no streaked stars in this image. The yellow ellipse (which is so narrow as to appear as a line here) indicates the 3σ positional uncertainty at the reference time of this mosaic as derived from the (A_1, A_2, A_3) $g(r)$, $g(r) \propto 1/r^2$ solution of Micheli et al. (2018). The red (very narrow) ellipse uses the same semimajor axes of the yellow ellipse, but is inflated by a factor of three to capture ephemeris dispersions caused by the different non-gravitational models and data weight assumptions in Micheli et al. (2018). The brightest pixel blobs that fall within these ellipses have signal-to-noise ratio (S/N) = 1–2 (0.1–0.2 μJy); the brightest blobs in this entire image have S/N = 2–3 (0.2–0.3 μJy). North is up and east is left. This image has a width of 55″ and a height of 50″. The effective pixels here are 0.86 arcsec, and the native pixel scale of IRAC is 1.21 arcsec.

implies that there is correlated noise somewhere in our data stream. The final image has residuals from background stars not fully removed from the mosaics, which cause some streaking across the image. There are likely also fainter cosmic rays and other low-level array effects that survive our filtering and enter into the final image. These residuals get smeared out because of the offsets and mapping between the instrument pixels and the final image pixels on a smaller scale that will lead to correlated "noise". The final image does not look like an image with only random pixel values in each pixel, but is consistent with what we would expect for the object of interest being too faint to detect. Alternately, this could be a tenuous detection of 'Oumuamua at 1σ, or around 0.1 μJy. In the analysis below, we use a 3σ upper limit for our calculations, which implies non-detection, or, at best, a weak detection.

There is no significant vignetting in the 4.5 μm IRAC channel near the edge of the field. However, there could be an impact on sensitivity from the object being off the edge of the detector for some frames due to the dithering. The 3σ position uncertainty ellipse shown in yellow in Figure 3 is fully covered by all exposures to within 2% of the median coverage of the central region (small variations are caused by rejection of bad pixels or pixels affected by background objects or cosmic rays during the exposures). To the right of the yellow ellipse, the coverage drops off roughly linearly along the red path until the end where it reaches a value of around 12% lower coverage than the central part of the image. Therefore, at that extreme end, the upper limit flux would then be 0.32 μJy for objects at this position in the mosaic. The coverage is similar along lines perpendicular to the major axes of the ellipses shown in Figure 3. Given the small area affected and the small (<10%) difference we simply use the global 3σ (0.3 μJy) upper limit for our analysis below.

3. Thermal Modeling and Interpretation of the Non-detection

We rule out any detections of 'Oumuamua at greater than 3σ ($\lesssim$0.3 μJy). Given the geometry of the observations, we have created a model spectral energy distribution that fits the available data: this 4.5 μm upper limit and H_V (the solar system absolute magnitude in V band), which we take to be 22.4 (Meech et al. 2017) with an uncertainty of 0.09 (using the fractional uncertainty given in Meech et al. 2017). At 4.5 μm and 1–2 au from the Sun the flux from this object is generally dominated by thermal emission (Trilling et al. 2016)—modulo some low-level gas emission, as described below—so a non-detection provides an upper limit on diameter and a lower limit on albedo.

We simulate the expected brightness of 'Oumuamua in *Spitzer* IRAC Channel 2 in order to interpret our upper limit detection. Using the Near-Earth Asteroid Thermal Model (NEATM; Harris 1998), we estimate the target's brightness as a function of its absolute magnitude H_V and a range in geometric albedo ($0.01 \leqslant p_V \leqslant 1.0$). Since the physical properties of 'Oumuamua are unknown, we consider a range of values for the thermal infrared beaming parameter: $0.8 \leq \eta \leq 2.5$. The justification for these values, which span the range of plausible

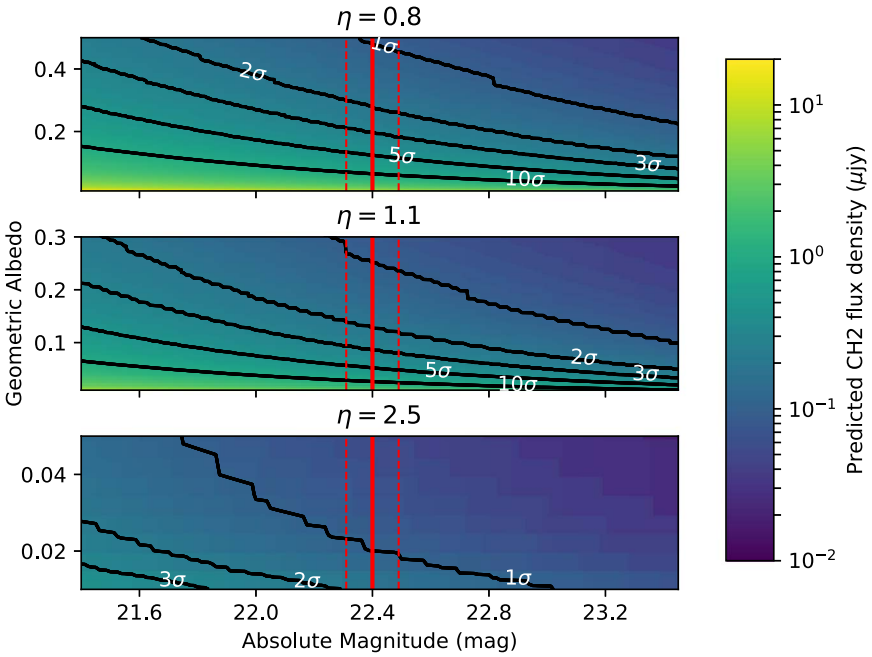

Figure 4. NEATM IRAC Channel 2 (CH2) flux density prediction for 'Oumuamua as a function of the target's absolute magnitude and its geometric albedo. The color scale represents different flux densities; black lines indicate levels of flux density as measured from our observations. The vertical lines indicate $H_V = 22.4 \pm 0.09$ (solid line and dashed lines on both sides). Solutions for three different η values are given, as indicated and described in the text. Low η requires high albedo, while $\eta = 2.5$ allows any albedo.

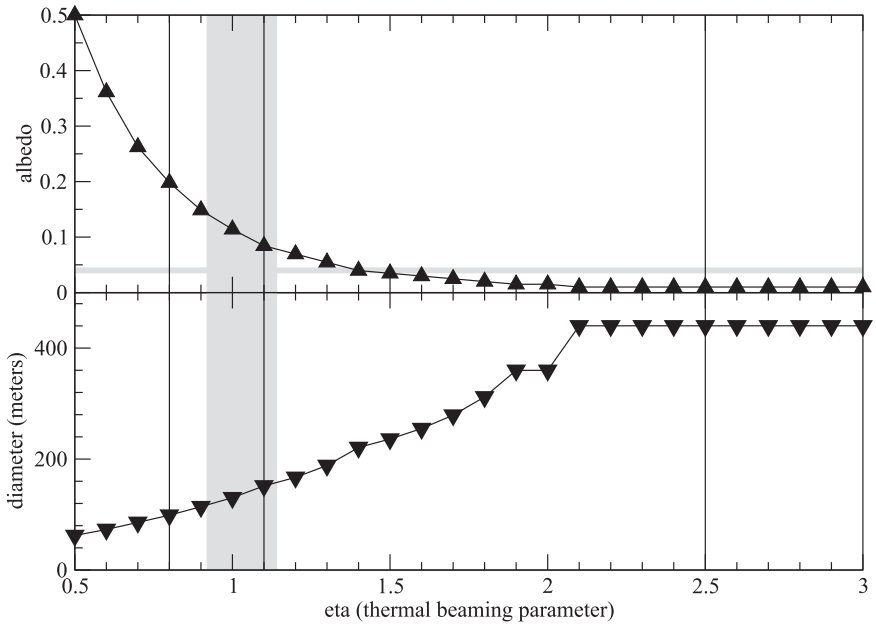

Figure 5. Albedo and effective spherical diameter solutions as a function of η. Our solutions shown here (lower limits for albedo as upward solid triangles in the upper panel, upper limits for diameter as downward open triangles in the lower panel) correspond to the 3σ detection thresholds described in the text and shown in Figure 4. The three representative cases shown in Figure 4 have $\eta = [0.8, 1.1, 2.5]$ (thin vertical black lines). The typical comet albedo of 0.04, as assumed by Micheli et al. (2018), is shown as the horizontal gray line in the top panel. The range of η values for comets (Fernandez et al. 2013) is shown as the broad vertical gray bar in both panels. The expected result is therefore the intersection of these two gray regions, with values of $\eta \approx 1$, albedo of 0.04, and diameter around 140 m; this result is discordant with our results. For $\eta > 2.0$, formally any albedo is allowed, and we choose here $p_V = 0.01$ as the smallest possible value that allows a finite diameter. (The non-smooth diameter function at $\eta = 2$ is simply an artifact of these vanishing solutions.) Assuming a shape elongation of 6:1 (McNeill et al. 2018), the physical dimensions of 'Oumuamua can be calculated as 180 × 1080 m for the low albedo case ($\eta = 2.5$) and 40 × 240 m for the high-albedo case ($\eta = 0.8$) for the short and long end-to-end dimensions, respectively.

η values for almost all NEOs (Trilling et al. 2016) and comets (Fernandez et al. 2013), is given in Section 4.3. We account for the target's geometry at the time of our *Spitzer* observations and contributions from reflected solar light in IRAC Channel 2 (Mueller et al. 2011), assuming an infrared to optical reflectance ratio of 1.4 (Trilling et al. 2016). Furthermore, we account for color corrections of the thermal component of the target's flux.

Figure 4 shows the distribution of predicted IRAC Channel 2 flux densities for the three different beaming parameters η.

Black lines indicate levels that are equal to integer multiples of the flux density noise level measured from our data. For $\eta = [0.8, 1.1, 2.5]$, the 3σ lower limit on the target's geometric albedo is [0.2, 0.1, 0.01], respectively (Figure 5). (Technically, any albedo is allowed for the $\eta = 2.5$ case; we set here the minimum value to be 0.01 to allow for finite diameters.) Correspondingly, we find a diameter upper limit of [98, 140, 440] m, respectively (Figure 5).

4. Discussion

4.1. Search for Activity

Based on the discovery of non-gravitational accelerations acting upon the orbit of 'Oumuamua (Micheli et al. 2018), we investigate the possibility of dust and gas activity in this object during our observations. Our non-detection enables the placement of upper limits on the production rates of dust, as well as CO and CO_2 gas; we are unable to constrain the production of other gas species. We use the same formalism that we used in detecting cometary behavior in the NEO Don Quixote (Mommert et al. 2014c)—Bauer et al. (2015) used similar approaches with *WISE* data—and our measured 3σ 4.5 μm flux density limit (0.3 μJy). Within a 6 pixel (5.2 arcsec) radius aperture (our standard size) we derive $Af\rho \leqslant 0.07$ cm following the definition of A'hearn et al. (1984), where A is albedo, f is the filling factor, and ρ is the linear radius of the emission (here, an upper limit). Assuming a dust particle radius of 10 μm, a dust bulk density of 1 g cm^{-3}, an albedo of 0.03 that is comparable with cometary dust and compatible with the range of possible albedos that we derived for 'Oumuamua, and a dust ejection velocity equal to the expansion velocity of gas at this distance from the Sun (Ootsubo et al. 2012), we find a 3σ upper limit on the dust production rate of 9 kg s^{-1}. Similarly, we calculate the 3σ upper limit on the CO_2 gas production rate as 9×10^{22} molecules s^{-1}. This can be scaled into a 3σ upper limit for the production of CO ($\sim 9 \times 10^{21}$ molecules s^{-1}) based on the ratio of the CO_2 and CO fluorescence efficiencies (Crovisier & Encrenaz 1983).

This CO upper limit is much lower than the Micheli et al. (2018) value of 4.5×10^{25} molecules s^{-1} (the most sensitive search in the literature) and implies that the outgassing from 'Oumuamua cannot have CO (or, presumably, CO_2) as a significant component, though the Micheli et al. (2018) CO production rate assumes a relative large body and albedo of 4%. If 'Oumuamua's size were 10–20 times smaller than the Micheli et al. (2018) diameter of 220 m, then the amount of CO outgassing at the upper limit would produce sufficient acceleration. However, an effective spherical diameter of 10–20 m would require an unacceptably high albedo and unacceptably low η, as described below, so this argument is rejected. Overall, we find these upper limit production rates and our upper limit of $Af\rho$ to be very low compared to the ensemble of comets (A'Hearn et al. 1995; Ootsubo et al. 2012), supporting the inactivity of 'Oumuamua during our observations.

4.2. Uncertainties

Our analysis of 'Oumuamua's physical properties is based on a measured flux density upper limit and thermal modeling performed with the NEATM. This model has been specifically designed for use on near-Earth asteroid observations and has been shown to be reasonably accurate over a wide range of cases (Harris et al. 2011; Mommert et al. 2018). It is applicable to thermal emission from any airless body and has been used extensively for comet nuclei as well (Lisse et al. 2005, 2009; Fernandez et al. 2013). A more sophisticated thermophysical model (Mommert et al. 2014a, 2014b, 2018) is not appropriate here due to the lack of information on the target (e.g., spin pole orientation and complex rotation state; shape is somewhat known but not uniquely so) and the upper-limit nature of the flux density measurement.

'Oumuamua is known to have a high-amplitude light curve (e.g., Jewitt et al. 2017; Knight et al. 2017; Meech et al. 2017; Bolin et al. 2018; Micheli et al. 2018) with, most likely, a period of 6–8 hr. Since our observations spanned 33 hr (clock time), any light curve effects are smoothed out, and we observe only the average flux. Furthermore, even though the *Spitzer* viewing geometry of 'Oumuamua is very different from that seen by observatories on and near the Earth, because 'Oumuamua is in an excited rotation state (Belton et al. 2018; Drahus et al. 2018; Fraser et al. 2018), we likely observed the same time-averaged projected surface area that would have been seen from Earth. Furthermore, the light curves presented in Belton et al. (2018) are not sinusoidal but rather have broad maxima and narrow minima, so our 33 hr integration is likely not corrupted by faint epochs in the light curve. Even in the case of a 55 hr period, one possible solution suggested by Belton et al. (2018), our observations span a significant fraction of the entire rotation and therefore included something close to the time-averaged cross-sectional area, except in the case of a pathological orientation.

We do not include uncertainties on the ratio of infrared to optical reflectances, as the impact of this ratio barely affects the overall results of this study, especially in the light of the large uncertainties on the beaming parameter η and hence the geometric albedo p_V.

We investigate the applicability of NEATM for this study given the high aspect ratio of 'Oumuamua (Meech et al. 2017; McNeill et al. 2018) and the assumption of sphericity in NEATM. For this purpose, we use an asteroid thermophysical model (Mommert et al. 2014a, 2014b, 2018) to derive the thermal and reflected solar flux density of the body, assuming both a highly elongated shape and a highly oblate shape (following Belton et al. 2018). Based on McNeill et al. (2018), we assume a triaxial ellipsoidal shape with semimajor axes 6:1:1 for the highly elongated shape and $1{:}\sqrt{6}{:}\sqrt{6}$ for the highly oblate shape, both in arbitrary units. Furthermore, we use the geometry during our *Spitzer* observations, the period (7.34 hr) derived by Meech et al. (2017), and assume a geometric albedo of 0.03 (in agreement with our NEATM-derived lower limit) and typical small-body values for thermal inertia and surface roughness. We simulate the flux density observed at *Spitzer* over one-quarter of the target's rotation and derive the average flux density, which is the quantity measured in our observations by combining all available data. Finally, we form the ratio of the average flux density derived for a spherical body (NEATM assumption) to the average flux density derived from the elongated shape and oblate shape models. Deriving this ratio minimizes the effects of the choice of the geometric albedo, surface roughness, and thermal inertia used in the simulation.

We find that this flux density ratio varies as a function of the target's spin axis latitude (as a proxy for the aspect angle of our observations). In the case of the elongated shape, a spin axis

latitude of 90° (equator-on view), the ratio is 1, and rotational effects are averaged out during our observations. The ratio decreases to 0.5 for spin axis latitudes approaching 0 (pole-on view), which represents an extreme case. In the case of the oblate shape, we find ratios of around [0.5, 1, 2] for $\beta = [0, 32.7, 90]$ degrees, respectively. As no information on the spin axis orientation of 'Oumuamua is available, we use the average[15] latitude of 32°.7, leading to a flux density ratio of 0.5 for the elongated shape model and 0.7 for the prolate shape. This mismatch between the flux densities of the different shapes is insignificant compared to the uncertainties introduced by the lack of knowledge of the surface properties (η) of 'Oumuamua. We therefore conclude that our use of NEATM is acceptable. We also note that the uncertainties in the results from the H_V uncertainties are small compared to the uncertainties from our lack of constraints on η.

4.3. Discussion of Possible Solutions

4.3.1. Low-albedo Solution

Since 'Oumuamua is in an excited rotation state, absorption of solar energy could be significantly more uniform around the surface than for rotation around a single axis. This implies the temperature distribution would be smoother than a single axis rotator, requiring a higher η than would otherwise be appropriate (Myhrvold 2016). The influence of the excited rotation state on the thermal emission of 'Oumuamua is difficult to model given our ignorance on its exact rotation state and overall shape. The extreme of the high η case would be represented by the Fast Rotator thermal model (FRM; Mommert et al. 2018). The FRM for this case produces virtually the same result as $\eta = 2.5$ (Figure 4). While the FRM is technically not suitable for complex rotation, it should be a reasonable approximation (especially since the rotation period is not very short).

Under the conservative assumption of $\eta = 2.5$ (the high η solution) any albedo is allowed (Figures 4 and 5). This includes arbitrarily low values. A comet-like value of 0.04 (Lamy et al. 2004), as was assumed in Micheli et al. (2018), implies a diameter of 220 m, and D-type asteroids have similarly low albedos (Thomas et al. 2011). This relatively large body can still experience non-gravitational accelerations but requires relatively large impulses and, consequently, relatively high activity rates that are not commensurate with our CO/CO_2 outgassing limits presented above.

4.3.2. Mid-range Albedo Solution

The default approach used in our *Spitzer* NEO program is to derive η from phase angle; Trilling et al. (2016) present in some detail the correlation and dispersion in the correlation between those two parameters. In this case, the phase angle of 31° implies η around 1.1. This value yields $p_V > 0.1$ and diameter less than 140 m. These values are intermediate in the range of acceptable solutions for 'Oumuamua (Figure 5). However, even this moderate albedo is generally inconsistent with cometary albedos.

4.3.3. High-albedo Solution

Finally, a lower η value appears to be more appropriate for comets (Fernandez et al. 2013). As our bounding case we take $\eta = 0.8$. This implies diameter less than 98 m and albedo greater than 0.2 (Figure 5). This small size is preferred from an activity and non-gravitational acceleration perspective, but the high albedo is unexpected since radiolysis of the surface during its interstellar passage would presumably have darkened the surface (and reddened it; a red color is indeed observed). One possible explanation is that 'Oumuamua's recent passage by the Sun was sufficient to emplace a thin layer of bright, fresh ice on the surface, as discussed below.

If 'Oumuamua has a high albedo then its inferred size (98 meter diameter) is substantially smaller than the 220 meter diameter that was assumed by Micheli et al. (2018), and its mass is smaller by the cubed ratio of these solutions ($(98/220)^3 = 1/11$). With a smaller mass, greater acceleration is produced for a given force (i.e., outgassing). However, force is proportional to the production rate, and the CO production rate derived here is 10^4 times less than that used by Micheli et al. (2018) to explain the measured astrometry. This rules out the the possibility that CO or CO_2 outgassing was responsible for the non-gravitational acceleration that Micheli et al. (2018) detected. However, we cannot put constraints on outgassing of water ice, which is the other main volatile ice found in comets, using our data (see below).

4.4. Summary of Results and a Possible Interpretation

There are several possible interpretations of our results, as follows. We note that in all cases, given our upper limit on CO and CO_2 production rates, some other gas species (e.g., water) must also have been emitted to explain the non-gravitational acceleration observed by Micheli et al. (2018). We can place no constraint on these other gas species.

(1) 'Oumuamua could have a high η, which would not be unusual for asteroids but would be very unusual for comets—although a body in an excited rotation state might have a higher than expected η value. In the high η case, the albedo is low, which means the diameter is large. However, a large body implies a large outgassing rate, which we do not see for CO and CO_2 and for dust. Conversely, (2) 'Oumuamua could have a low η, in accordance with expectations for cometary bodies. However, this requires an albedo that is much higher than that expected for comets. This high albedo corresponds to a small diameter, which is favored, considering our upper limits on gas and dust production. (3) Intermediate values of η, albedo, and diameter are also possible, though these are not really consistent with any expectations.

In conclusion, there is no simple asteroidal or cometary physical model that agrees with expectations and previous work (including non-gravitational acceleration) and our results for all of η, albedo, and diameter. One plausible explanation is that 'Oumuamua was a dormant comet nucleus reactivated, after millions of years in interstellar space, by heating during its close passage by the Sun. This reactivation either destroyed the thin dark mantle expected to be created by cosmic rays and galactic ultraviolet radiation (e.g., Lisse et al. 1998, 2004) and/or coated the surface with an optically thick layer of new, fresh

[15] To compute this average, we assume a uniform distribution of spin poles on the sphere of the body. This is obtained by uniform sampling in longitude and uniform sampling in the sine of the latitude. Now we compute the average of latitude knowing that sine of latitude is uniform. The average from −1 to 1 is zero (since this distribution is symmetric), but if we take only the northern hemisphere (for example) then we calculate $\int_0^1 \arcsin(x)dx$, which is 32°.7. We note that even under other assumptions of the average value, the deviation from our nominal solutions is insignificant in all cases.

ice. In the latter case, the bright coating could plausibly have come from CO, CO_2, or water, as follows.

We assume that 'Oumuamua is outgassing 9×10^{22} molecules of CO_2 per second (see above). In the high-albedo case, the effective spherical diameter of 'Oumuamua is around 98 m, and the surface area is therefore around 3×10^4 m^2 (taking 49 m as the radius of the equivalent sphere). If we require a uniform surface layer that is 10 μm thick—so that the surface appears bright with CO_2 ice for observations made at 4.5 μm—then the volume of this surface layer is around 0.3 m^3.

The density of CO_2 ice is approximately 1.5 g cm^{-3}. The mass required to create a surface layer of 0.3 m^3 is therefore 4.5×10^5 g. We calculate the number of CO_2 molecules required as

$$\frac{4.5 \times 10^5 \text{ g}}{44 \text{ g/mole}} \times 6.02 \times 10^{23} \text{ molecules/mole},$$

which is around 6×10^{27} molecules of CO_2. Given the CO_2 upper limit of 9×10^{22} molecules s^{-1} derived above, depositing 6×10^{27} molecules of CO_2 requires only around 67000 s, or around 0.8 days—far less than the few weeks of 'Oumuamua's perihelion passage time. Thus, even if the efficiency of this process is small, it is still quite plausible that a low level of activity—induced by solar heating of a near-subsurface CO_2 reservoir—could produce enough material to coat the surface with bright, fresh CO_2 and increase the albedo to the relatively high value required in our high-albedo case.

Alternately, heating of water ice into gas could present a plausible scenario. Cometary dust to gas ratios are typically around 5:1, so our dust emission upper limit of 9 kg s^{-1} corresponds to 1.8 kg s^{-1} as an upper limit for gas emission. If we assume that all of this gas emission is in H_2O, then we find

$$\frac{1.8 \times 10^3 \text{ g s}^{-1}}{18 \text{ g/mole}} \times 6.02 \times 10^{23} \text{ molecules/mole},$$

which is around 6×10^{25} molecules s^{-1}, enough to produce the non-gravitational accelerations reported by Micheli et al. (2018).

CO+CO_2 ice in typical solar system comets is around 15% of the water abundance. Here our limits imply around 0.15% for this ratio—a factor of 100 times smaller. This could imply that 'Oumuamua was heated to $\sim$100 K prior to our observations—either by our Sun, or before entering our solar system. 'Oumuamua, if propelled by water ice sublimation at 6×10^{25} molecules s^{-1} while producing only $\leqslant 9 \times 10^{22}$ molecules s^{-1} of CO+CO_2, must therefore have been previously devolatilized of these more volatile ices.

4.5. Possible Analogies

Unfortunately, we do not have pre-perihelion observations to compare to these post-perihelion observations to test the hypothesis that 'Oumuamua brightened during its perihelion passage. Further modeling of 'Oumuamua's outgassing—whether CO, CO_2, or some other species—would be very beneficial.

A plausible analogy for such activity-produced resurfacing is the well-studied comet 67P, the target of the Rosetta mission. Keller et al. (2017) and Liao et al. (2018) showed that the nucleus of 67P was partially resurfaced through re-condensation of volatiles released from the nucleus; Liao et al. (2018) found that the deposition rate of water ice could be up to several microns in an hour near perihelion. While this does not correspond directly to low levels of activity and an albedo increase, as proposed here for 'Oumuamua, it is nevertheless evidence that activity can resurface small-body surfaces after perihelion passage, at the order of magnitude required for 'Oumuamua (1–10 μm deposited in days or weeks). Bolin et al. (2018) saw no color changes as a function of rotation, which could imply a relatively uniform resurfacing process. This suggested emission must be too small to create a measurable change in velocity after the first 'Oumuamua observations (i.e., the beginning of the observational arc), or else occurred after perihelion but before the discovery observation of 'Oumuamua (see Figure 1), in order to be consistent with the results reported in Micheli et al. (2018).

Another possible analogy is the well-studied comet Shoemaker-Levy 9. Sekanina (1995) shows that after the breakup of this body from tidal forces exerted by Jupiter, many fragments appeared intrinsically brighter—as if fresh ice had just been revealed or deposited onto their surfaces. It is possible that the shape and/or rotation state of 'Oumuamua were affected by its passage near the Sun, and interior volatiles may also have been liberated onto the surface at the same time.

5. Conclusions

We observed interstellar body 'Oumuamua for 30 hr of integration time at 4.5 μm with the *Spitzer Space Telescope*. We did not convincingly detect the object and place upper limits on its flux during our observations. Depending on the assumptions used in our thermal model, we find low-, medium-, and high-albedo solutions (and corresponding limits on the effective spherical diameter). We do not detect any activity from 'Oumuamua and place upper limits for CO and CO_2 emission that are far lower than were derived by Micheli et al. (2018) under the assumption of a body with 4% albedo; we can place no constraints on emission of other gas species (e.g., water ice). The nature of the gas emission and the origin of the non-gravitational accelerations are still unknown.

It is not clear what type of body in our solar system is the most similar to 'Oumuamua, as there are significant failures with both comets and primitive (D-type) asteroids as end-member analogs. One possible scenario that appears to explain many of the observed properties of 'Oumuamua, including our observations, is exposure or creation, from outgassing, of a fresh, icy, bright surface due to thermal reactivation during 'Oumuamua's close perihelion passage in 2017 September. However, due to the geometry of 'Oumuamua's passage through the solar system, there will be no more observations of this object, so it is likely that we will never know the true nature of this interstellar interloper.

This work is based in part on observations made with the *Spitzer Space Telescope*, which is operated by the Jet Propulsion Laboratory, California Institute of Technology under a contract with NASA.

We thank the SSC Director for approving these DDT observations and the SSC staff for rapidly implementing these observations with their usual technical excellence. Part of this research was conducted at the Jet Propulsion Laboratory, California Institute of Technology, under a contract with NASA. K.M. acknowledges support from NSF awards AST1413736 and AST1617015.

Facility: Spitzer(IRAC).

Software: MOPEX (Makovoz et al. 2006), IRACproc (Schuster et al. 2006).

ORCID iDs

David E. Trilling https://orcid.org/0000-0003-4580-3790
Michael Mommert https://orcid.org/0000-0002-8132-778X
Joseph L. Hora https://orcid.org/0000-0002-5599-4650
Davide Farnocchia https://orcid.org/0000-0003-0774-884X
Sean Carey https://orcid.org/0000-0002-0221-6871
Carey M. Lisse https://orcid.org/0000-0002-9548-1526
Steven R. Chesley https://orcid.org/0000-0003-3240-6497
Yanga R. Fernandez https://orcid.org/0000-0003-1156-9721
Massimo Marengo https://orcid.org/0000-0001-9910-9230
H. A. Weaver https://orcid.org/0000-0003-0951-7762
Karen Meech https://orcid.org/0000-0002-2058-5670
Marco Micheli https://orcid.org/0000-0001-7895-8209

References

A'Hearn, M. F., Millis, R. C., Schleicher, D. O., et al. 1995, Icar, 118, 223
A'hearn, M. F., Schleicher, D. G., Millis, R. L., et al. 1984, AJ, 89, 579
Bacci, P., Maestripieri, M., Tesi, L., et al. 2017, MPEC, 2017-U181
Bannister, M. T., Schwamb, M. E., Fraser, W. C., et al. 2017, ApJL, 851, L38
Bauer, J. M., Stevenson, R., Kramer, E., et al. 2015, ApJ, 814, 85
Belton, M. J. S., Hainaut, O. R., Meech, K. J., et al. 2018, ApJL, 856, L21
Bolin, B. T., Weaver, H. A., Fernandez, Y. R., et al. 2018, ApJL, 852, L2
Crovisier, J., & Encrenaz, T. 1983, A&A, 126, 170
Ćuk, M. 2018, ApJL, 852, L15
Do, A., Tucker, M. A., & Tonry, J. 2018, ApJL, 855, L10
Dones, L., Brasser, R., Kaib, N., et al. 2015, SSR, 197, 191
Drahus, M., Guzik, P., Waniak, W., et al. 2018, NatAs, 2, 407
Fazio, G. G., Hora, J. L., Allen, L. E., et al. 2004, ApJS, 154, 10
Feng, F., & Jones, H. R. A. 2018, ApJL, 852, L27
Fernandez, Y. R., Kelley, M. S. P., Lamy, P., et al. 2013, Icar, 226, 1138
Fitzsimmons, A., Snodgrass, C., Rozitis, B., et al. 2018, NatAs, 2, 133
Fraser, W. C., Pravec, P., Fitzsimmons, A., et al. 2018, NatAs, 2, 383
Gaidos, E. 2018, MNRAS, 477, 5692
Harris, A. W. 1998, Icar, 131, 291
Harris, A. W., Mommert, M., Hora, J. L., et al. 2011, AJ, 141, 75
Jackson, A. P., Tamayo, D., Hammond, N., et al. 2018, MNRAS, 478, L49
Jewitt, D., Luu, J., Rajagopal, J., et al. 2017, ApJL, 850, L36
Katz, J. I. 2018, MNRAS, 478, L95
Keller, H. U., Mottola, S., Hviid, S. F., et al. 2017, MNRAS, 469, S357
Knight, M. M., Protopapa, S., Kelley, M. S. P., et al. 2017, ApJL, 851, L31
Lamy, P., Toth, I., Fernandez, Y. R., & Weaver, H. A. 2004, in Comets II, ed. M. C. Festou, H. U. Keller, & H. A. Weaver (Tucson, AZ: Univ. Arizona Press), 223
Liao, Y., Marschall, R., Su, C. C., et al. 2018, P&SS, 157, 1
Lisse, C. M., A'hearn, M. F., Groussin, O., et al. 2005, ApJL, 625, L139
Lisse, C. M., A'Hearn, M. F., Hauser, M. G., et al. 1998, ApJ, 496, 971
Lisse, C. M., Beichman, C. A., Bryden, G., & Wyatt, M. C. 2007, ApJ, 658, 584
Lisse, C. M., Fernandez, Y. R., A'Hearn, M. F., et al. 2004, Icar, 171, 444
Lisse, C. M., Fernandez, Y. R., Reach, W. T., et al. 2009, PASP, 121, 968
Lisse, C. M., Sitko, M. L., Marengo, M., et al. 2017, AJ, 154, 182
Makovoz, D., Roby, T., Khan, I., & Booth, H. 2006, Proc. SPIE, 6274, 62740C
Masiero, J. 2017, arXiv:1710.09977
McNeill, A., Trilling, D. E., & Mommert, M. 2018, ApJL, 857, L1
Meech, K. J., Weryk, R., Micheli, M., et al. 2017, Natur, 552, 378
Micheli, M., Farnocchia, D., Meech, K., et al. 2018, Natur, 559, 223
Milani, A., Sansaturio, M. E., Tommei, G., Arratia, O., & Chesley, S. R. 2005, A&A, 431, 729
Mommert, M., Farnocchia, D., Hora, J. L., et al. 2014a, ApJL, 789, L22
Mommert, M., Hora, J. L., Farnocchia, D., et al. 2014b, ApJ, 786, 148
Mommert, M., Hora, J. L., Harris, A. W., et al. 2014c, ApJ, 781, 25
Mommert, M., Jedicke, R. J., & Trilling, D. E. 2018, AJ, 155, 74
Mueller, M., Delbo', M., Hora, J. L., et al. 2011, AJ, 141, 109
Myhrvold, N. 2016, PASP, 128, 962
Ootsubo, T., Kawakita, H., Hamada, S., et al. 2012, ApJ, 752, 15
Raymond, S. N., Armitage, P. J., & Veras, D. 2018a, ApJL, 856, L7
Raymond, S. N., Armitage, P. J., Veras, D., et al. 2018b, MNRAS, 476, 3031
Schuster, M. T., Marengo, M., & Patten, B. M. 2006, Proc. SPIE, 6270, 627020
Sekanina, Z. 1995, A&A, 304, 296
Thomas, C. A., Trilling, D. E., Emery, J. P., et al. 2011, AJ, 142, 85
Trilling, D. E., Mommert, M., Hora, J., et al. 2016, AJ, 152, 172
Trilling, D. E., Mueller, M., Hora, J. L., et al. 2010, AJ, 140, 770
Trilling, D. E., Robinson, T. D., Roegge, A., et al. 2017, ApJL, 850, L38
Ye, Q.-Z., Zhang, Q., Kelley, M. S. P., & Brown, P. G. 2017, ApJL, 851, L5
Zwart, S. P., Torres, S., Pelupessy, I., et al. 2018, MNRAS, 479, L17